Climate Simulation for 125 kyr BP with a Coupled Ocean–Atmosphere General Circulation Model

MARISA MONTOYA AND HANS VON STORCH

Institute of Meteorology, University of Hamburg, Hamburg, Germany

THOMAS J. CROWLEY

Department of Oceanography, Texas A&M University, College Station, Texas

(Manuscript received 19 October 1998, in final form 10 May 1999)

ABSTRACT

The ECHAM-1 T21/LSG coupled ocean–atmosphere general circulation model (GCM) is used to simulate climatic conditions at the last interglacial maximum (Eemian, 125 kyr BP). The results reflect the expected surface temperature changes (with respect to the control run) due to the amplification (reduction) of the seasonal cycle of insolation in the Northern (Southern) Hemisphere. A number of simulated features agree with previous results from atmospheric GCM simulations (e.g., intensified summer southwest monsoons) except in the Northern Hemisphere poleward of 30°N, where dynamical feedbacks in the North Atlantic and North Pacific increase zonal temperatures about 1°C above what would be predicted from simple energy balance considerations. As this is the same area where most of the terrestrial geological data originate, this result suggests that previous estimates of Eemian global average temperature might have been biased by sample distribution. This conclusion is supported by the fact that the estimated global temperature increase of only 0.3°C greater than the control run has been previously shown to be consistent with CLIMAP sea surface temperature estimates. Although the Northern Hemisphere summer monsoon is intensified, globally averaged precipitation over land is within about 1% of the present, contravening some geological inferences but not the deep-sea $\delta^{13}C$ estimates of terrestrial carbon storage changes. Winter circulation changes in the northern Arabian Sea, driven by strong cooling on land, are as large as summer circulation changes that are the usual focus of interest, suggesting that interpreting variations in the Arabian Sea sedimentary record solely in terms of the summer monsoon response could sometimes lead to errors. A small monsoonal response over northern South America suggests that interglacial paleotrends in this region were not just due to El Niño variations.

1. Introduction

Coupled general circulation models (GCMs) are the state-of-the-art tools to simulate climate under certain boundary conditions and its response to changes in these, and to study its variability. Coupled GCMs have been used in the past decade to assess potential climate change in response to increased atmospheric greenhouse gas levels. All models include a number of adjustments to reproduce satisfactorily the present observations. Hence, an accurate simulation of the present climate does not guarantee a correct performance of the model under different boundary conditions. The validation of GCMs in this case is provided by the simulation of past climates and the comparison of the results to the evidence from the geological record, which, in addition, may provide explanations of the reconstructed climatic features and estimates of the climate sensitivity.

Most efforts in this line have focused on the late Quaternary (0–20 kyr BP), a period for which the reconstructed paleodata are abundant and accurately dated. Paleoclimate simulations and sensitivity studies have shed light on the orbital control and the influence of surface boundary conditions and CO_2 on climate (Kutzbach and Guetter 1986; Prell and Kutzbach 1987; Kutzbach and Liu 1997), in particular at the mid–early Holocene (Kutzbach and Gallimore 1988; Mitchell et al. 1988; Hewitt and Mitchell 1996, 1998; Hall and Valdes 1997; Kutzbach et al. 1998) and at the last glacial maximum (LGM) (Ganopolski et al. 1997; Dong and Valdes 1998; Bush and Philander 1998), and on the role of vegetation feedbacks in past climate changes (Crowley and Baum 1997; Kutzbach et al. 1996; Texier et al. 1997; Ganopolski et al. 1998; Kubatzki and Claussen 1998).

We have used a coupled ocean–atmosphere GCM to simulate climate conditions at 125 kyr BP, the maximum of the last interglacial period (the Eemian, ~120–130

Corresponding author address: Dr. Marisa Montoya, Potsdam Institute for Climate Impact Research, PO Box 60 12 03, 14412 Potsdam, Germany.
E-mail: montoya@pik-potsdam.de

TABLE 1. Boundary conditions.

	CO_2 (ppmv)	Eccentricity	Obliquity (°)	Angle of perihelion (°)
Control run	330	0.017	23.45	282.16
125 kyr BP	267	0.040	23.79	127.27

kyr BP). The last interglacial is covered in western and southern Europe by several long pollen sequences, all of which show three warm periods correlated with the warm marine isotopic stages 5a, 5c, and 5e: Padul in southern Spain (Pons and Reille 1988), the Lac du Bouchet and the Velay Maars in the French Massif Central (de Beaulieu and Reille 1992), Les Echets near Lyon (de Beaulieu and Reille 1984), La Grande Pile (Woillard 1978), Monttichio (Watts 1985) and Valle di Castiglione (Follieri and Sadori 1988) in Italy, and Tenaghi Philippon (Wijmstra 1969) and Ioaninna (Tzedakis 1993) in Greece. Evidence for warmth from land, ice, and in a smaller number ocean records from mid–high northern latitudes [see Fig. 3 in LIGA Members (1991)] and for sea level up to 6 m higher than present (Mesolella et al. 1969; Bloom et al. 1974; Ku et al. 1974) have led to the widespread assumption that the last interglacial was possibly the warmest time period of the last 200 000 yr in terms of global temperature, and to regard this and other interglacial periods from the late Quaternary as analogs for a future potentially warmer world due to rising greenhouse gas levels (Kellogg 1977; Fung et al. 1988; Budyko and Izrael 1991; Zubakov and Borzenkova 1990; Shabalova and Können 1995).

This experiment constitutes the first attempt to use a coupled ocean–atmosphere GCM to simulate the climate of the last interglacial, shedding light on the role of the ocean in the climate response to the perturbed radiative forcing. Previous climate simulations of this period have been carried out with energy balance models (EBMs; Crowley and Kim 1994) and atmospheric general circulation models (AGCMs) with ocean boundary conditions prescribed to modern values (Royer et al. 1984; Prell and Kutzbach 1987; Kutzbach et al. 1991; de Noblet et al. 1996) or coupled to static mixed layer ocean models (Harrison et al. 1995).

The paper is organized as follows: section 2 describes the experimental setup. Section 3 describes results concerning the temporal evolution of the sea ice, atmosphere, and ocean systems; the seasonal and mean annual differences with respect to the control run in the large-scale atmospheric fields and the hydrological cycle; and the mean annual differences in the ocean circulation. Section 4 compares the coupled GCM thermal response to that obtained by a two-dimensional EBM in order to highlight the changes due to thermodynamic or dynamic interactions. Finally, section 5 summarizes and discusses the main results, focusing on the comparison against previous climate simulations and against the evidence from the geological record.

2. Experimental setup

a. The climate model

The climate model used in this experiment (hereafter, the Eemian run) is the ECHAM-1 T21/LSG coupled ocean–atmosphere GCM (Cubasch et al. 1992). This model has been used in one of the few millennia coupled runs performed at the moment (von Storch et al. 1997), which constitutes our control run, and in several climate change experiments (Cubasch et al. 1992, 1994).

The atmospheric component (ECHAM-1) (Roeckner et al. 1992) is based on a low-resolution version of the European Centre for Medium-Range Weather Forecasts (ECMWF) model adapted for climate study purposes. It is a spectral model with a horizontal resolution given by a triangular cutoff at zonal wavenumber 21 (ca. 5.6° $\times$ 5.6°). Vertically, the model is discretized in a hybrid σ–p coordinate system with 19 levels. The time integration is semi-implicit with a time step of 40 min. Prognostic variables are vorticity and divergence, temperature, surface pressure, water vapor, and cloud water. Subgrid-scale processes are parameterized. The diurnal cycle is included. The runoff into the ocean is calculated using a simple surface hydrology model. The calving of glaciers is not considered; an attempt is made to correct the error caused by the accumulation of snow over glaciers using the flux correction for freshwater flux (see below).

The oceanic component is the Large Scale Geostrophic (LSG) model (Maier-Reimer et al. 1993), which is based on an approximation of the primitive equations for large-scale geostrophic motion. It has 11 variably spaced levels in the vertical and a horizontal E grid formed by two overlapping 5.6° $\times$ 5.6° grids. The nonlinear advection of momentum is neglected, and fast gravity waves are damped by an implicit time integration scheme with a time step of 30 days, which is reduced to 1 day for the computation of sea ice, temperature, and salinity at the two uppermost ocean levels to resolve the response of the upper ocean to the synoptic variability of the atmosphere. Salinity and heat transport are computed with an upstream advection scheme. A small explicit horizontal diffusion is introduced to counteract the tendency for mode splitting in the horizontal E grid. Vertical convective mixing occurs whenever the stratification becomes unstable. Sea ice is computed from the ice heat balance and the advection by oceanic currents, using a simplified viscous rheology. A realistic bottom topography is included.

Before coupling, the ocean model was integrated for

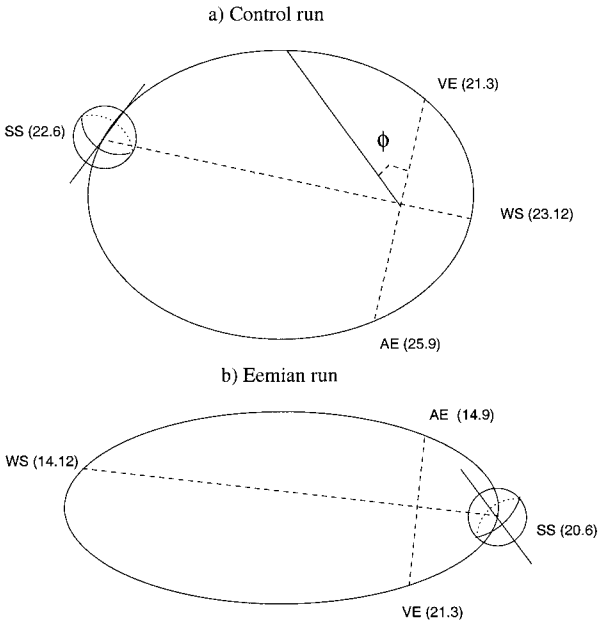

FIG. 1. Position of the solstices and equinoxes (a) for the control run (the present), and (b) the Eemian run (125 kyr BP). Dates of solstices and equinoxes are given in parenthesis: VE, vernal equinox; AE, autumnal equinox; SS, summer solstice; WS, winter solstice.

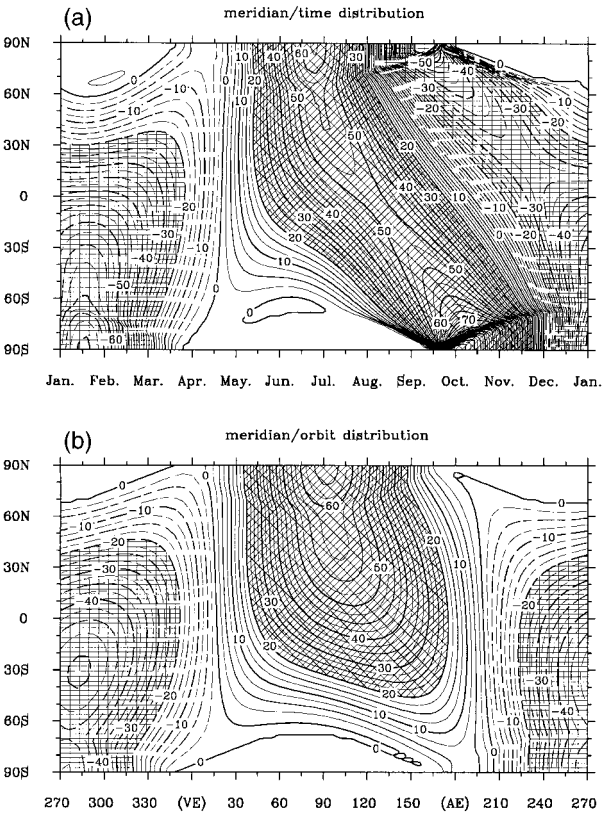

FIG. 2. (a) Time vs lat and (b) celestial long vs lat differences in zonally averaged incoming solar radiation at the top of the atmosphere (125 kyr BP minus present, W m^{-2}).

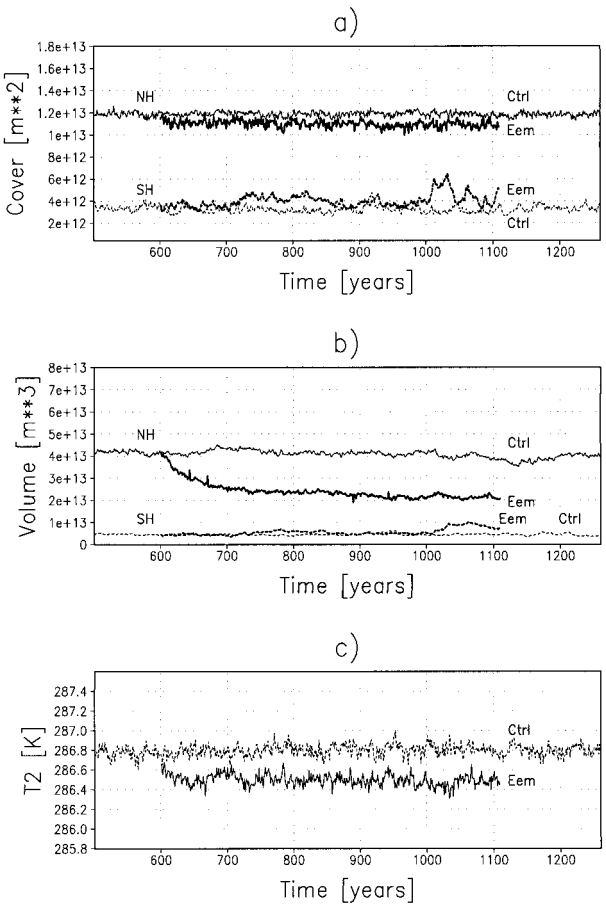

FIG. 3. Time series of the (a) annual mean total sea ice extent (m^2), (b) annual mean total sea ice volume (m^3), and (c) globally averaged near-surface (2 m) temperature (K), in the Northern (solid line) and Southern Hemispheres (dashed line), for the control (thin line) and Eemian runs (thick line).

5000 yr in a spinup run driven by monthly climatological wind stress fields (Hellerman and Rosenstein 1983), and a feedback to an effective monthly mean air temperature constructed from the Comprehensive Ocean–Atmosphere Data Set (Woodruff et al. 1987) and the annual mean surface salinity (Levitus 1982). The freshwater fluxes diagnosed from this run, together with the same wind stress and air temperature forcing as used before, were used as external forcing for a subsequent integration of 2000 yr.

At this stage, the LSG model was coupled to the ECHAM-1 model. Both were integrated synchronously, coupled through the air–sea fluxes of momentum, heat (sensible, latent and radiative), and freshwater (precipitation minus evaporation, plus runoff along the coastal boundaries). Using the sea surface temperature (SST) and the sea ice thickness as surface boundary conditions, the fluxes are computed by the atmospheric model at each 40-min time step, accumulated over the ocean time step and then transferred to the ocean model.

A flux correction is applied in order to minimize a

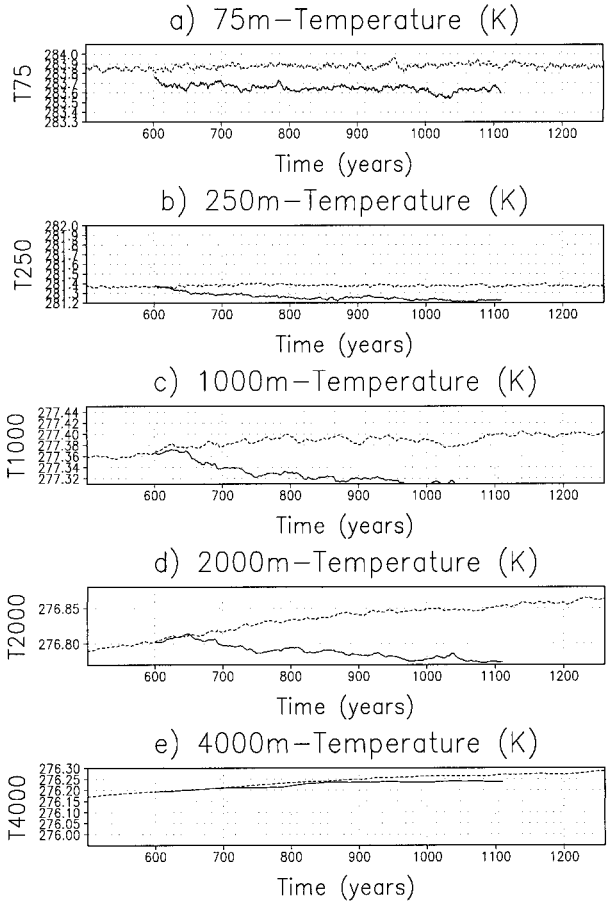

FIG. 4. Time series of the annual mean globally averaged temperature of the ocean at (a) 75-, (b) 250-, (c) 1000-, (d) 2000-, and (e) 4000-m depths for the control (dashed line) and Eemian runs (solid line) (K).

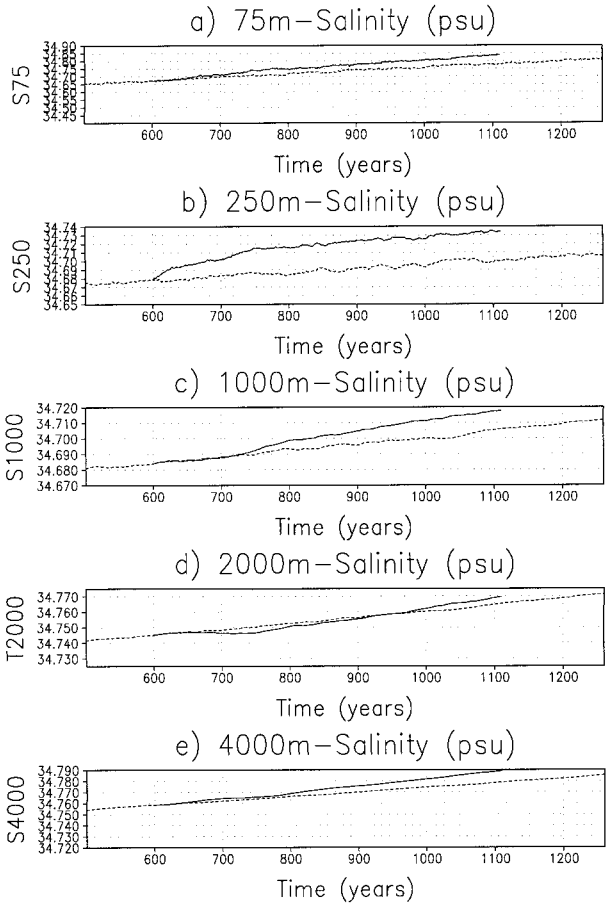

FIG. 5. Time series of the annual mean globally averaged salinity of the ocean at (a) 75-, (b) 250-, (c) 1000-, (d) 2000-, and (e) 4000-m depths for the control (dashed line) and Eemian runs (solid line) (psu).

climate drift of the coupled system away from the mean states simulated by the uncoupled models (Sausen et al. 1988). The flux correction is based in a linearization of the fluxes that couple the ocean and the atmosphere and for small perturbations should have no effect on the response of the climate, but its application in greenhouse warming simulations (Manabe et al. 1991; Manabe et al. 1992; Cubasch et al. 1992, 1995) has cast some doubt with respect to the internal consistency of such experiments. An assessment of the potential errors due to this technique would require a comparison to the true response of a coupled model without drift. However, sensitivity experiments with simple box models (Egger 1997) suggest that the performance of the flux correction is suspicious in climate simulations in which a transition to a new, different equilibrium state takes place, which is clearly not our case.

b. The external forcing

In the Eemian run the ECHAM-1 T21/LSG climate model was integrated for 510 yr starting at year 600 of the control run (von Storch et al. 1997). The CO_2 concentration was prescribed to 267 ppmv, consistent with mean levels for the last interglacial estimated from ice core measurements (Barnola et al. 1987), instead of 330 ppmv as in the control run, and insolation was changed by setting the earth's orbital parameters to their values at 125 kyr BP according to Berger (1978) (Table 1): the eccentricity of the earth's orbit was greater, obliquity was slightly greater, and, with the vernal equinox fixed at 20 March in both experiments, perihelion took place in northern summer (July) instead of in northern winter (January), as in the present (Fig. 1).

1) THE DEFINITION OF THE SEASONS

For given values of eccentricity and obliquity, insolation is a function of the true longitude Φ, that is, the angle measured counterclockwise from the vernal equinox (Fig. 1). Due to the variation of the earth's orbital parameters, the dates at which a given true longitude Φ is attained differ today and at 125 kyr BP (Kutzbach and Gallimore 1988; Joussaume and Braconnot 1997).

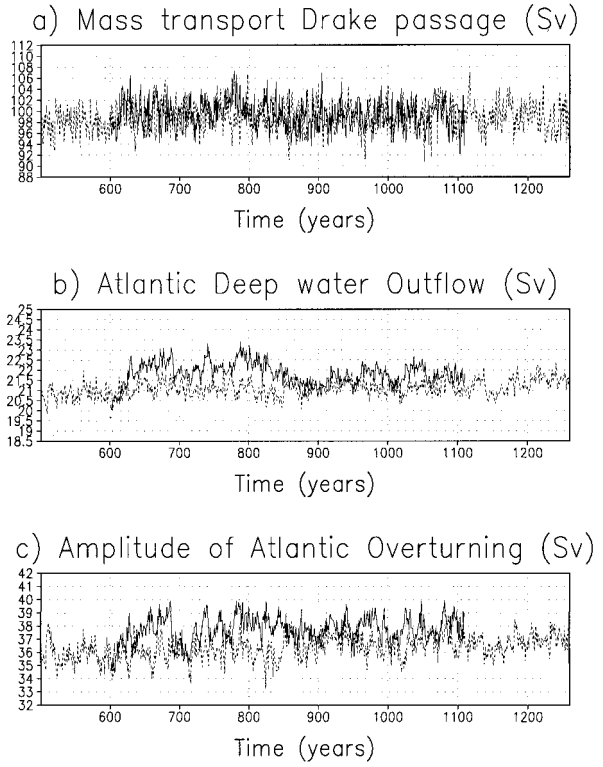

FIG. 6. Time series of (a) mass transport of the Antarctic Circumpolar Current (ACC) across the Drake Passage, (b) outflow of NADW at 30°S, and (c) amplitude of the Atlantic overturning circulation, defined as the maximum value of the zonally averaged mass transport streamfunction of the meridional overturning circulation in the Atlantic Ocean, for the control (dashed line) and the Eemian runs (solid line) (Sv).

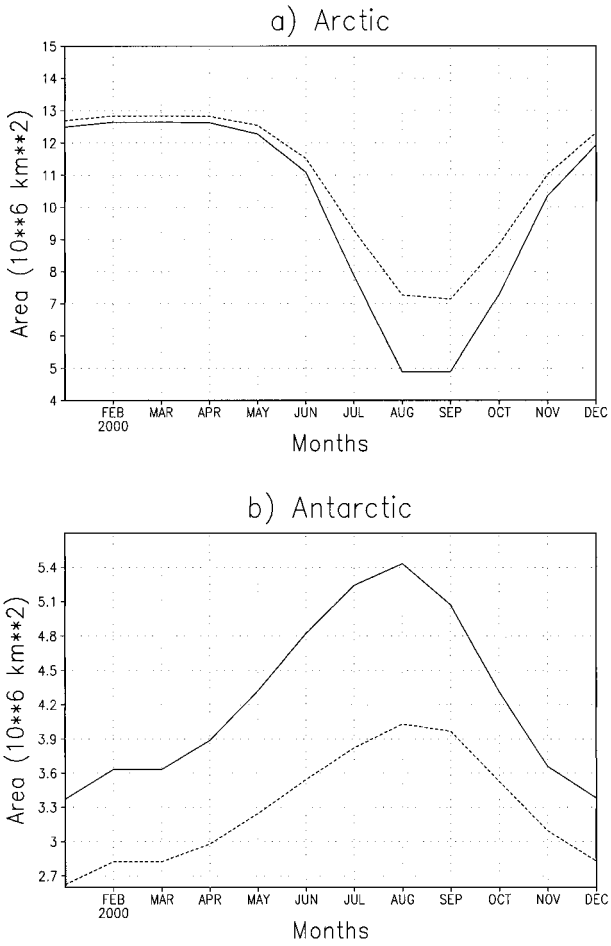

FIG. 7. Mean annual cycle of total (a) Arctic and (b) Antarctic sea ice cover (poleward of 65°N and 65°S, respectively) for the control (dashed line) and Eemian runs (solid line) (m^2).

To illustrate this, the dates of the solstices an equinoxes for both time periods are shown in Fig. 1 together with the time versus latitude and true longitude vs. latitude diagrams of zonally averaged differences (125 kyr BP minus present) in insolation (Fig. 2), fixing the vernal equinox to 20 March. In the vicinity of the vernal equinox, both representations are similar; the disagreements between them increase as we approach the autumnal equinox.

We have considered the orbit of the earth (Monin 1986) to redefine northern summer and winter as those periods that correspond to the same interval in Φ as June–August (JJA) and December–February (DJF) today. Although our results (not shown) indicate that the difference between JJA and DJF means and our redefined means is small compared to the difference fields between the Eemian and the present, we have adopted the latter in our summer and winter definitions. Hence, northern summer and winter are here defined as the periods between days 150 and 231, and days 320 and 59, respectively, in our 360-day model. For the control run the definitions of summer and winter are the usual ones.

2) CHANGES IN INCOMING SOLAR RADIATION

At 125 kyr BP, as a consequence of the combined effects of the timing of perihelion and the greater obliquity, northern summer insolation was enhanced with respect to present at all latitudes (Fig. 2), with a peak value of 60 W m^{-2} at high northern latitudes. On average, insolation increased by 50 W m^{-2} (12%). Winter insolation in turn decreased at all latitudes with an average value of 26 W m^{-2} (11%). At high latitudes the decreasing effect on insolation of the timing of perihelion was partly compensated by the greater obliquity. Hence, maximum northern winter insolation decreases took place at subtropical southern latitudes.

To summarize, the seasonal cycle of insolation was amplified in the Northern Hemisphere and attenuated in the Southern Hemisphere. Mean annual insolation increased at high latitudes, where enhanced summer insolation is not offset in winter, and decreased at low latitudes, but was below 2 W m^{-2} at all latitudes (not shown), and its globally averaged change was negligible (0.23 W m^{-2}).

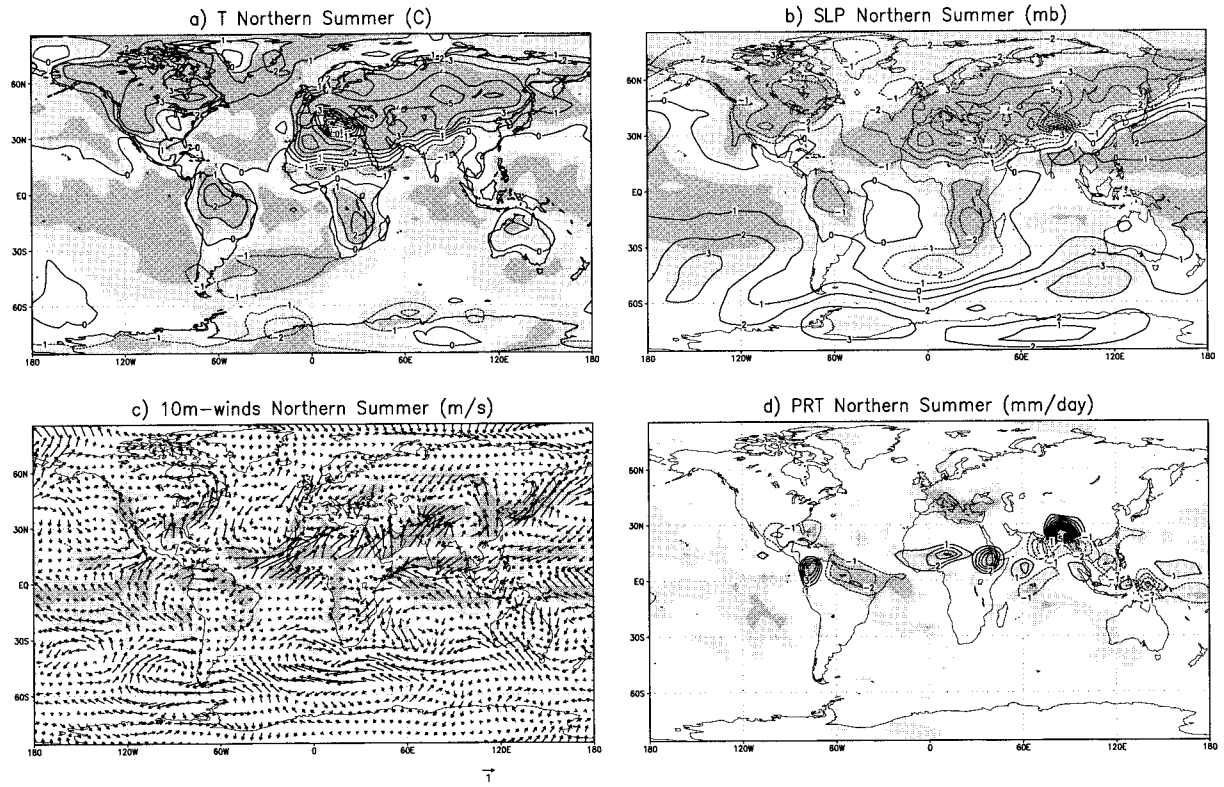

FIG. 8. Mean simulated difference (Eemian minus control run) in northern summer (a) near-surface temperature (°C), (b) sea level pressure (mb), (c) 10-m winds (m s^{-1}), and (d) total precipitation (mm day^{-1}). Shading indicates the level of local recurrence p. Light shading, $p \geq 0.8$ or $p \leq 0.2$; heavy shading, $p \geq 0.95$ or $p \leq 0.05$.

3. Results

a. Temporal evolution

The temporal evolution of the sea ice, atmosphere, and ocean systems in the control run are fully described in von Storch et al. (1997). After the change of the external forcing in year 600 of the control run to Eemian conditions, the sea ice and the near-surface temperature require slightly more than 100 yr to attain quasi-stationary equilibrium (Fig. 3). The globally averaged temperature of the upper layers of the ocean have not completely reached equilibrium after 510 yr, but the trend is below -0.1°C $(400\ \text{yr})^{-1}$ at all levels down to 1000-m depth (Fig. 4). In the deep ocean a nearly constant trend in globally averaged temperature is found both in the Eemian and in the control run (Fig. 4). This could be explained if the deep ocean had not completely reached equilibrium before its coupling to the atmosphere model (von Storch et al. 1997). A trend in globally averaged salinity was also found at all levels in both runs (Fig. 5), consistent with a small negative globally integrated freshwater flux [ca. -0.07 Sverdrup $\equiv 10^6\ \text{m}^3\ \text{s}^{-1}$ (Sv)]. However, this does not have any severe influence on the ocean dynamics: the typical indices that characterize the dynamical state of the ocean (Fig. 6) show some signs of oscillations subsequent to the external forcing change, but reach a quasi-stationary state after 200–300 yr. After that the Drake Passage transport is almost unchanged whereas the Atlantic Deep Water Outflow and the North Atlantic Deep Water (NADW) are enhanced by 0.5 Sv and 2 Sv relative to the control run mean values of 20.5 and 35 Sv, respectively.

b. Sea ice

The increase of summer insolation at high northern latitudes at 125 kyr BP [section 2b(2) translates into enhanced net surface solar radiation (not shown). SSTs increase and Arctic sea ice cover is reduced; this response is amplified through the positive sea ice albedo–SST feedback, and is not limited to northern summer but takes place all year round (Fig. 7; results show mean values averaged over the last 300 yr of each run). At high southern latitudes winter insolation at 125 kyr BP remained equal to the present while summer insolation decreased (Fig. 2); the surface solar radiation decreases in the annual mean and sea ice thickness and extent are enhanced all year round (Fig. 7).

c. Large-scale atmospheric patterns

This section describes the difference (Eemian minus control run) in the mean large-scale atmospheric sim-

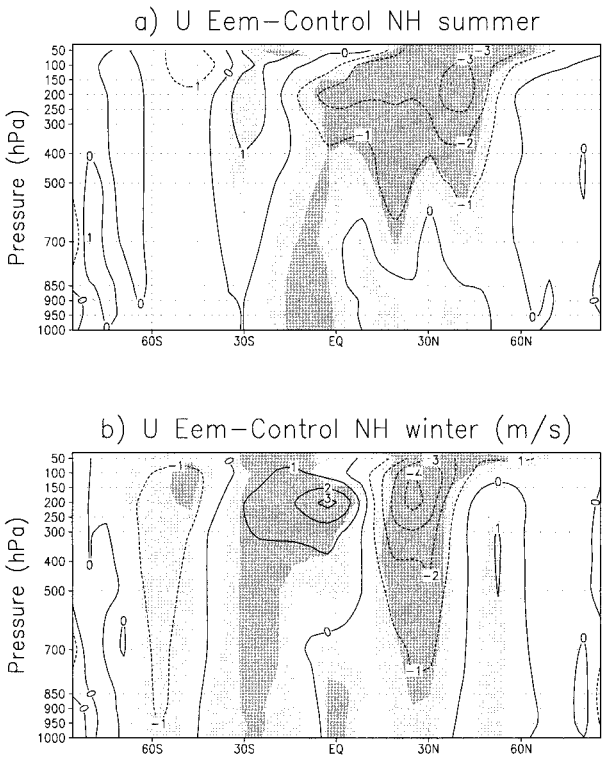

FIG. 9. Difference (Eemian minus control run) in mean zonally averaged zonal velocity (m s^{-1}). Shading indicates the level of local recurrence p. Light shading, $p \geq 0.8$ or $p \leq 0.2$; heavy shading, $p \geq 0.95$ or $p \leq 0.05$.

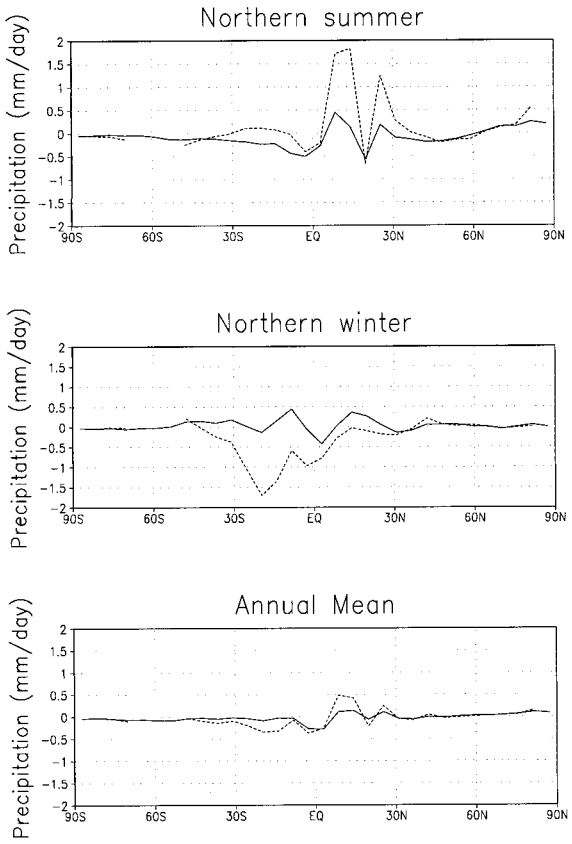

FIG. 10. Difference (Eemian minus control run) in mean zonally averaged precipitation over land (dashed line) and over land plus ocean (solid line) (mm day^{-1}).

ulated fields in summer and winter, averaged over the final 300 yr of each run. A test for statistical significance of the mean differences is not meaningful: due to the high statistics, negligible differences will outcome statistically significant. Rather, a univariate recurrence analysis was applied to the simulated atmospheric fields to test for physical significance of their mean differences (von Storch and Zwiers 1998) (see the appendix). Physically non-negligible local differences correspond to extreme values of the local level of recurrence p, which is indicated by shading: light shading refers to $p \geq 0.8$ or $p \leq 0.2$ and heavy shading refers to $p \geq 0.95$ or $p \leq 0.05$ (see Figs. 8, 9, 11, and 12 later).

1) NORTHERN SUMMER

In northern summer, the increase of insolation and surface solar radiation (not shown) causes overall enhanced near-surface temperatures over land with maximum values above 4°–5°C in the northern continents, where the increase in radiative forcing and the landmass distribution are greatest (Fig. 8a). Due to the larger heat capacity of the oceans, SST change is less than 1°C except at high northern latitudes, where they are amplified through sea ice albedo–SST positive feedback (section 3b). The only near-surface temperature decreases over land (2°–3°C) take place in central Africa and south Asia and are related to enhanced evaporation and cloudiness in these areas (not shown).

Sea level pressure (SLP) (Fig. 8b) reflects the thermally direct response to the temperature changes, decreasing over the warmer landmasses, especially over Eurasia, North Africa, and North America, and increasing over the surrounding cooler oceans, especially over the Southern Ocean and northwestern Pacific. The land–ocean surface pressure gradient is hence enhanced and, thereby, the low-level convergence and moisture transport into both regions (Fig. 8c). Precipitation increases in equatorial Africa by about 6 mm day^{-1} (Fig. 8d). In south Asia, the low-level south westerly flow is shifted northward and easterly surface wind anomalies appear over the Arabian Sea, south Asia, and the northern Indian Ocean, while southwesterly anomalies are found over the Arabian Sea and north India (Fig. 8c); moisture transport farther inland is enhanced, giving rise to a slight decrease of precipitation in south India and a significant increase in the Tibetan region (Fig. 8d), reflecting a northward migration of the large-scale convergent flow.

In the present climate, the summer monsoon at upper levels (not shown) is characterized by the onset of an anticyclone over south Asia, as is seen from the 200-

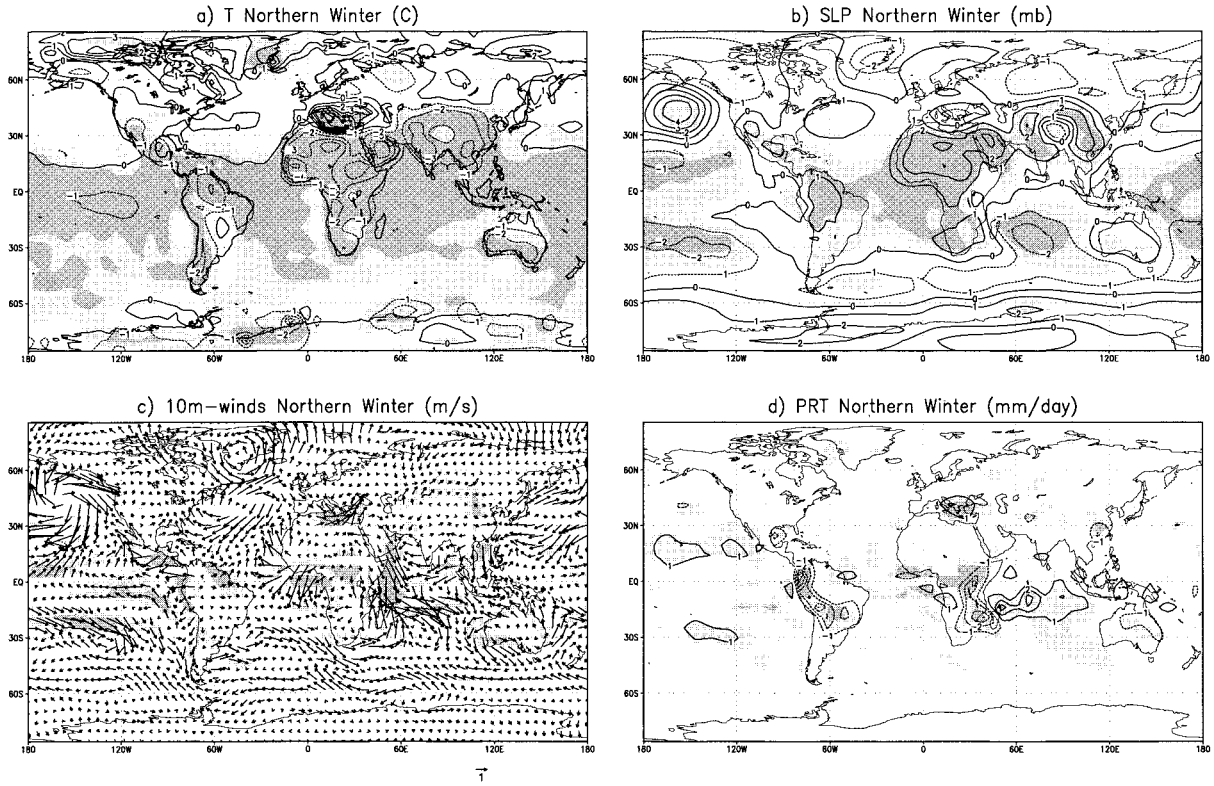

FIG. 11. Mean simulated difference (Eemian minus control run) in northern winter (a) near-surface temperature (°C), (b) sea level pressure (mb), (c) 10-m winds (m s^{-1}), and (d) total precipitation (mm day^{-1}). Shading indicates the level of local recurrence p. Light shading, $p \geq 0.8$ or $p \leq 0.2$; heavy shading, $p \geq 0.95$ or $p \leq 0.05$.

mb streamfunction. In addition, the 200-mb velocity potential field χ shows a region of large-scale divergence ($\chi < 0$) over the western Pacific, which is associated with a convection center, and large-scale convergence over the eastern Atlantic. These features, which are satisfactorily captured in the control run (not shown), are perturbed in the Eemian run in several ways: the 200-mb streamfunction and the 200-mb velocity potential pattern are both shifted northwestward, and the meridional gradient of the 200-mb streamfunction is enhanced over south Asia (not shown); the result are enhanced upper-level easterlies throughout the whole northern Tropics, reflecting an intensification of the tropical easterly jet (Fig. 9a). Precipitation over northern South America is also enhanced (Fig. 8d), mainly due to enhanced convection. Hence, the above results reflect an intensification and redistribution of the monsoonal circulation in the Northern Hemisphere caused by the enhanced land–sea temperature contrast.

The insolation perturbation causes an attenuation of the meridional temperature gradient in the northern midlatitudes that translates into an attenuation of the zonal component of the midlatitude westerly flow at all levels, in particular at the core of the jet stream (Fig. 9a).

Finally, changes of total precipitation in regions other than those affected by the monsoonal circulation have a much smaller amplitude and are spatially complicated. The zonally averaged precipitation over land only and over land plus ocean (Fig. 10) reflects the aforementioned changes in the monsoon circulation in the Tropics, but only minor differences in extratropical regions. As a result of enhanced evaporation, the northern continents were drier in summer except in regions affected by the summer monsoon (not shown).

2) NORTHERN WINTER

In northern winter, consistent with the decrease of insolation and net surface solar radiation at almost all latitudes, cooling is found south of 30°N (Fig. 11a). Maximum near-surface temperature decreases occur in the northern subtropical continents. The southern subtropical landmasses, however, show a more moderate cooling. As a consequence of the enhanced summer insolation at high northern latitudes (see section 3b) warming up to 4°C takes place. However, midnorthern latitudes also show a moderate warming that might as well reflect changes in heat transport associated to changes in the ocean circulation (see section 3e).

SLP (Fig. 11b) increases over the colder subtropical landmasses of both hemispheres and decreases over the surrounding southern oceans. The land–sea pressure

contrast is thereby enhanced in the Northern Hemisphere, while reduced in the Southern Hemisphere. Strong outflow takes place over central Africa and south Asia (Fig. 11c), causing enhanced low-level convergence and precipitation over the Indian Ocean at about 20°S (Fig. 11d). At the same time, precipitation decreases up to 4 mm day^{-1} over the subtropical southern continents (South America, south Africa, and Australia). These results reflect a weakening of the southern summer monsoon and a very strong northern monsoon response.

The midlatitude meridional temperature gradient is also reduced in winter, leading to decreased westerly flow at all levels (Fig. 9b). At southern midlatitudes the opposite effect takes place, and the tropical easterly jet is reduced, which together with the fact that circulation patterns are shifted northward translates into westerly anomalies over the tropical Atlantic Ocean (Fig. 9b).

Another consequence of the reduced meridional temperature gradient is an attenuation of the baroclinic instability that originates the formation of midlatitude synoptic-scale disturbances (storm tracks), whose intensity is reduced. Since their passage generates variability on the 2–6-day timescale, they can be characterized by the peak values of the intraseasonal standard deviation of the bandpass (2.5–6 days) geopotential height at 500 mb. Although severely underestimated in the control run, their location over the North Atlantic and North Pacific is well captured (Fig. 12a). Results shown are restricted to winter in the Northern Hemisphere, for which changes with greatest amplitude are obtained, reflecting their attenuation over the North Atlantic and North Pacific (Fig. 12b).

3) ANNUAL MEAN

Despite the large warming simulated in northern summer, significant cooling occurs in winter, with the net result that the mean annual temperature changes (not shown) are lower than 1°C almost everywhere, and the difference (Eemian minus control) in mean annual globally averaged temperature is −0.32°C (Table 2). In a similar way, the strong Asian winter monsoon overcompensates its intensification in summer, and mean annual simulated features (e.g., surface winds in the Arabian Sea, not shown) reflect the winter rather than the summer response.

The simulated globally averaged precipitation on land is reduced by 1% (Table 3). Mean annual precipitation minus evaporation ($P - E$) also decreases in the annual mean over most of eastern Asia and North America (not shown), and globally $P - E$ over land is reduced (Table 4), with the opposite increase over the oceans; hence, moisture transport from the ocean to the land decreased globally at the Eemian with respect to the control.

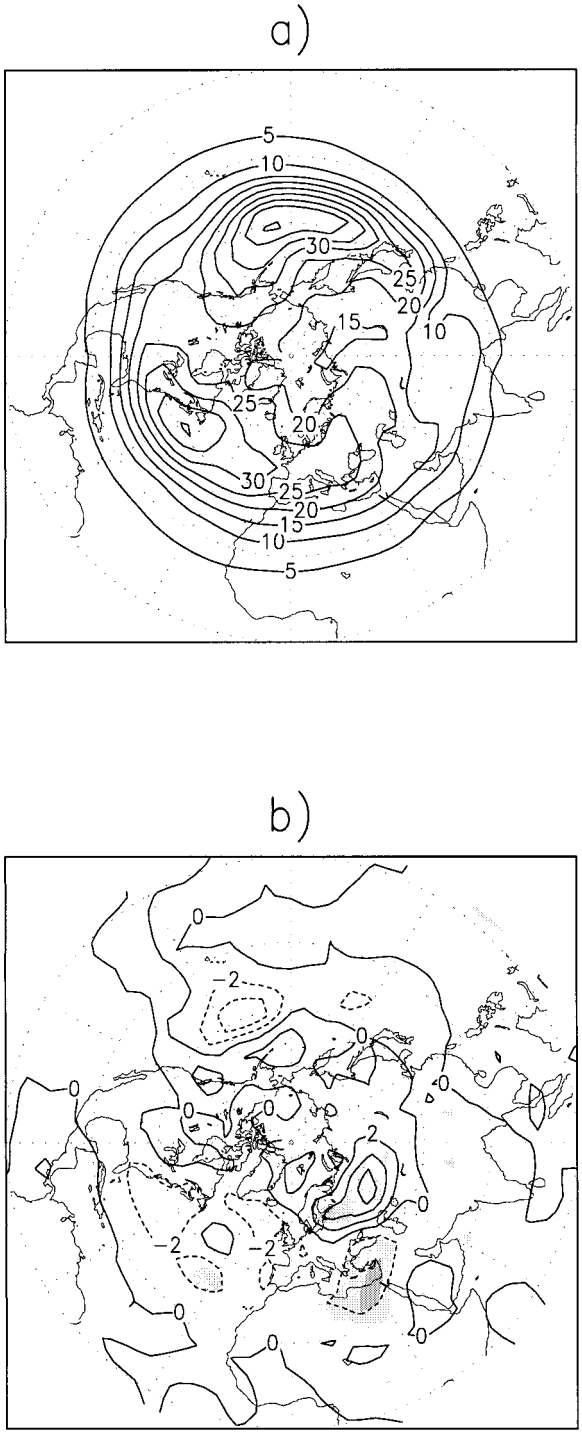

FIG. 12. Intraseasonal standard deviation of the bandpass geopotential height at 500 mb in winter (DJF) for (a) the control run and (b) the difference Eemian minus control run (m).

d. Temperature differences from present

The aforementioned simulated change in globally averaged near-surface temperature (−0.32°C, Table 2) contrasts with the common assumption that the Eemian

TABLE 2. (First row) Difference (Eemian minus control) in mean simulated near-surface temperature for selected areas (global, Northern Hemisphere, 0°–30°N, 30°–90°N, 30°–90°N over land only, and for northern summer), and (second row) corrected values to compensate for the different CO_2 concentrations of our Eemian and control runs (°C).

	Global	NH	0°–30°N	30°–90°N	30°–90°N, L	30°–90°N L, NS
ΔT (°C)	−0.32	−0.15	−0.60	0.27	0.20	3.0
ΔT_{adj} (°C)	0.47	0.64	0.19	1.10	0.99	3.79

was the warmest time period in the last 200 kyr in terms of global temperature based in paleodata. Since these reflect deviations with respect to a preindustrial rather than present time period, and the control run was carried out with a CO_2 concentration of 330 ppm, about 60 ppmv higher than that used in the Eemian run, the simulated temperatures should be corrected to compensate for the radiative forcing introduced by these different CO_2 concentrations. The difference in radiative forcing between two levels of CO_2, C_1 and C_2, is approximately given by $\Delta F = 6.3 \log C_1/C_2$. For small radiative perturbations, the corresponding change in global temperature is approximately linear: $\Delta T = \lambda \Delta F$. Making use of the fact that the sensitivity of the ECHAM-1/LSG model is 2.6°C for a doubling of CO_2 the temperature correction is $\Delta T = 0.79$°C.

The difference in simulated mean annual near-surface temperature (Eemian minus control run) has also been calculated for several selected areas (Table 2): global, Northern Hemisphere, 0°–30°N, 30°–90°N, and 30°–90°N over land only (also in northern summer). The corrected values for the selected areas show that the warmer model temperatures occur in the same region where most of the paleodata are located, specially in northern summer. Thus, higher than present simulated mean annual temperatures in the Northern Hemisphere are consistent with the evidence from the paleodata from this region without necessarily implying a much higher globally averaged temperature, suggesting that the proxy temperature estimates could be geographically and seasonally biased.

e. Ocean circulation

Due to the large memory of the ocean it is not meaningful to apply a local recurrence test to the ocean simulated fields. The most significant difference in the mean horizontal barotropic (vertically averaged) streamfunction occurs in the Pacific Ocean (Fig. 13a), where the subtropical gyres are slightly intensified with respect to the control run.

A slight intensification (ca. 5%) of the meridional overturning circulation in the Atlantic Ocean is found at the Eemian with respect to the control run, with enhanced NADW formation compensated by increased inflow of warm waters at upper layers (Fig. 13b). The zonally averaged mass transport streamfunction of the meridional circulation is calculated only down to 30°S, where the ocean basin southern limits are set by the continental southern edges (see, e.g., Fig. 13a). This response is caused by the decreased freshwater flux north of 40°N in the Atlantic Ocean (Fig. 14) mainly due to an increase in evaporation in the entire North Atlantic Ocean (by ca. 0.02 Sv at 30°N), rather than to a decrease in precipitation or runoff (not shown), which overcompensates the enhanced surface stability expected from the high northern latitude warming.

In the Pacific Ocean (Fig. 13c) the difference in the mean overturning circulation shows an intensification of the Antarctic Bottom Water (AABW) inflow with enhanced upwelling at the surface, a similar response to that obtained by Kim et al. (1998). In addition, an anomalous cell flow showing intermediate water formation in the North Pacific is found: convection down to depths of about 2000 m at high northern latitudes is triggered as a result of the reduced integrated freshwater flux at all latitudes in the Pacific basin (Figs. 14a,b). This, in turn, is caused both by a direct decrease in $P - E$ over the North Pacific (e.g., at 15°–20°N evaporation and precipitation contribute with −0.04 and −0.02 Sv, respectively) and by changes and redistribution of precipitation and $P - E$ over southeast Asia: runoff into the Indian Ocean is enhanced at the expense of the northeastern Pacific (−0.02 Sv at 15°–20°N), enhancing the surface salinity in this region (not shown).

As a consequence of the changes in ocean circulation, the global northward heat transport by the ocean is enhanced (Fig. 15). The Pacific Ocean is the main con-

TABLE 3. Difference (Eemian minus control) in mean simulated precipitation for selected areas in northern summer, in northern winter, and in the annual mean (mm day^{-1}).

	Land	Sea	Globe	NH land	NH sea	NH globe	SH land	SH sea	SH globe
NW	−0.25	0.17	0.05	−0.05	0.14	0.07	−0.70	0.20	0.04
NS	0.15	−0.23	−0.12	0.24	−0.25	−0.06	−0.04	−0.21	−0.18
AM	−0.03	−0.04	−0.04	0.04	−0.02	0.00	−0.20	−0.04	−0.07

TABLE 4. Difference (Eemian minus control) in mean simulated precipitation minus evaporation ($P - E$) for selected areas in northern summer, in northern winter, and in the annual mean (mm day^{-1}).

	Land	Sea	Globe	NH land	NH sea	NH globe	SH land	SH sea	SH globe
NW	−0.15	0.10	0.03	−0.01	0.03	0.02	−0.47	0.15	0.04
NS	0.04	−0.06	−0.03	0.10	−0.02	0.03	−0.10	−0.10	−0.10
AM	−0.01	0.01	0.00	0.04	−0.02	0.01	−0.14	−0.02	−0.01

tributor to this change. The peak value of the change in northward heat transport (ca. 0.12 PW) is attained around 20°N for both the Pacific and global oceans.

4. Differences from linear response

One way to assess the results is to compare the thermal response to that of the EBM discussed by Kim et al. (1998). Significant differences between the two runs highlight the dynamical and thermodynamical feedbacks unique to the coupled model. Figure 16 shows the zonally averaged surface temperature change (Eemian minus control run) for each ocean basin and for the global ocean as simulated by the ECHAM-1/LSG coupled GCM compared to that obtained by a linear EBM. In order to compensate for the different CO_2 concentration in the Eemian and control GCM runs, the corresponding temperature change must be corrected for (ca. 0.79°C; section 3e).

The results indicate that the models are in fairly close agreement in the Southern Hemisphere and in the northern Tropics. However, at mid–high northern latitudes the GCM response is considerably warmer than would be predicted by a linear model. Two mechanisms may account for these discrepancies. First, the increased summer warming and melting of Arctic sea ice in the GCM Eemian run results in warmer winter temperatures

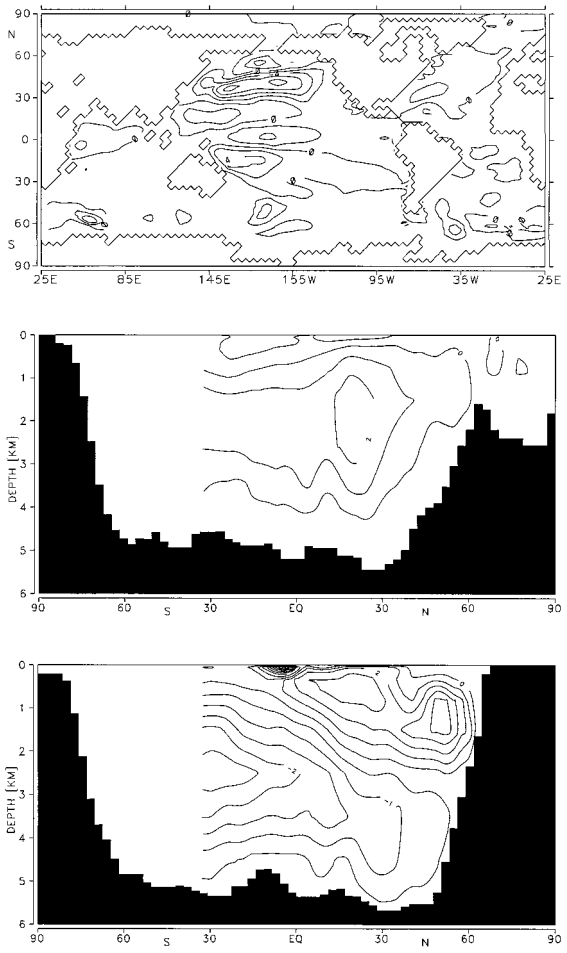

FIG. 13. Difference (Eemian minus control run) in mean (a) horizontal barotropic streamfunction, and (b) zonally averaged mass transport streamfunction of the meridional overturning circulation in the Atlantic Ocean and (c) in the Pacific Ocean, averaged over 300 yr (Sv).

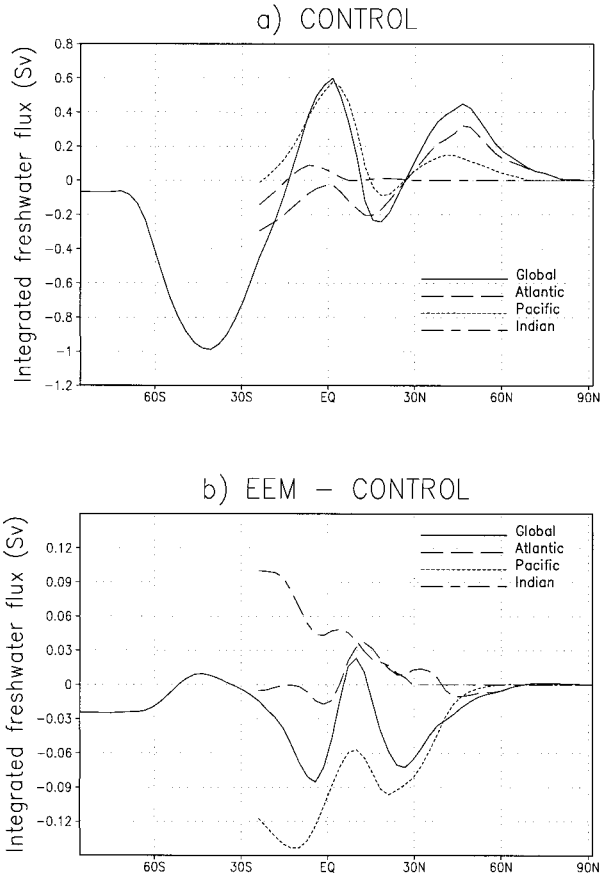

FIG. 14. Mean integrated freshwater flux from 90°N southward for the three ocean basins and the global ocean for (a) the control run and (b) the difference Eemian minus control run (Sv).

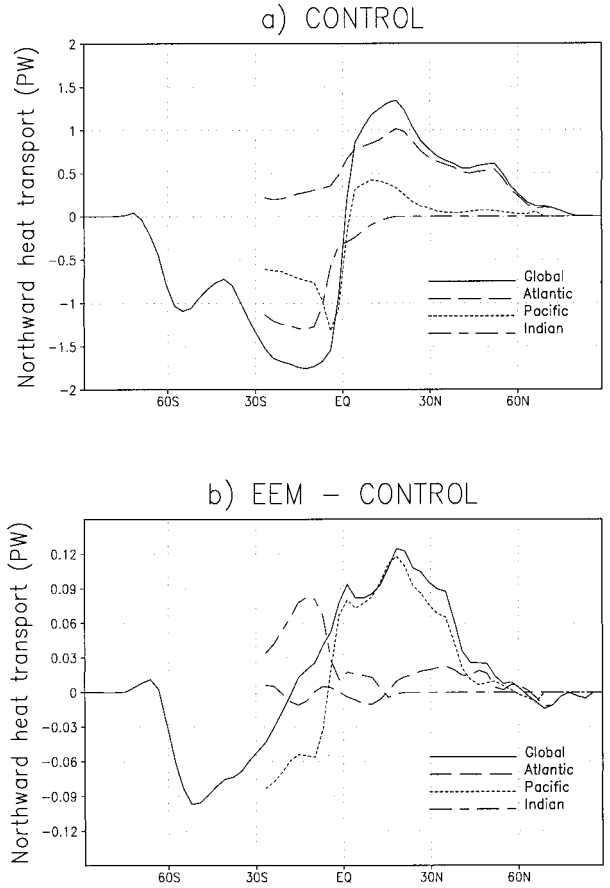

FIG. 15. Mean northward heat transport for the three ocean basins and the global ocean for (a) the control run and (b) the difference Eemian minus control run (PW).

than simulated by the EBM. Second, GCM-simulated changes in the surface and deep ocean circulation translate into a 10% increase of the northward heat transport by the ocean while changes in the heat transport by the atmosphere are negligible (not shown). Zonally averaged cloudiness changes are $\leq 1\%$, and hence cloudiness changes do not appear to play an important role.

5. Conclusions and discussion

Our results reflect the expected amplification of the seasonal cycle of temperatures in the Northern Hemisphere at the last interglacial, in close agreement with those of previous climate simulations for this and other time periods of the late Pleistocene with enhanced Northern Hemisphere summer insolation (''warm summer orbit periods'') by means of AGCMs with boundary conditions prescribed to modern values (Prell and Kutzbach 1987; de Noblet et al. 1996; Hewitt and Mitchell 1996) or coupled to mixed layer ocean models (Kutzbach and Gallimore 1988) and EBMs (Crowley and Kim 1994).

This thermal response has implications for the atmospheric circulation. First, the land–sea temperature contrast, and hence the land–sea surface pressure gradient, is enhanced in the Northern Hemisphere in both seasons. This affects features of the atmospheric circulation that are driven by differential heating, such as the monsoon circulation. The results qualitatively reflect an intensification of the summer southwest and African monsoon circulation and precipitation, which is consistent with the evidence from the geological record (Petit-Maire 1994) and with previous climate simulations of warm summer orbit periods of the late Pleistocene (Kutzbach and Guetter 1986; Kutzbach and Gallimore 1988; Mitchell et al. 1988). Features such as the northward migration of the large-scale convergent flow and the intensification of the tropical easterly jet are found as reported in AGCM simulations by Hewitt and Mitchell for 6 kyr BP (de Noblet et al. 1996; Hewitt and Mitchell 1996) and for 126 kyr BP (de Noblet et al. 1996). In turn, the summer southern monsoon is weakened, as found by Kutzbach and Guetter (1986) in their AGCM simulation for 9 kyr BP.

Convection over northern South America is also enhanced. This feature may be of interest because for the early Holocene precipitation changes on western South America have been interpreted in terms of changing El Niño–Southern Oscillation conditions (Rollins et al. 1986; Sandweiss et al. 1996). If similar monsoonal variations in northern South America occurred during the early Holocene, precipitation and circulation changes could complicate interpretations of some of the evidence (e.g., geomorphic features) used to infer changes in El Niño frequency in the region.

A second consequence of the thermal response is a reduction of the meridional temperature gradient at mid-northern latitudes in both seasons, which causes an attenuation of both the mean extratropical circulation and the baroclinic activity of the atmosphere. The opposite effects are found in the Southern Hemisphere.

Strong winter cooling translates into a very strong Asian winter monsoon, as seen in Hewitt and Mitchell (1996) and Kutzbach et al. (1998) so that its imprint in the annual mean is more important, and the simulated mean annual features reflect a reduction of the intensity of the monsoon rather than an enhancement.

In contrast with previous climate simulations of periods with enhanced Northern Hemisphere summer insolation such as 9 kyr BP, which show enhanced precipitation over the warmer Northern Hemisphere continents in northern summer, and decreased over the oceans (Kutzbach and Guetter 1986; Mitchell et al. 1988; Kutzbach and Gallimore 1988), precipitation changes over the extratropical regions are minor. As a result of enhanced evaporation, the northern continents were drier in summer except in regions affected by the summer monsoon. Mean annual precipitation minus evaporation ($P - E$) decreased over most of eastern Asia and North America (not shown). This result is at variance with other climate simulations for 125 kyr BP

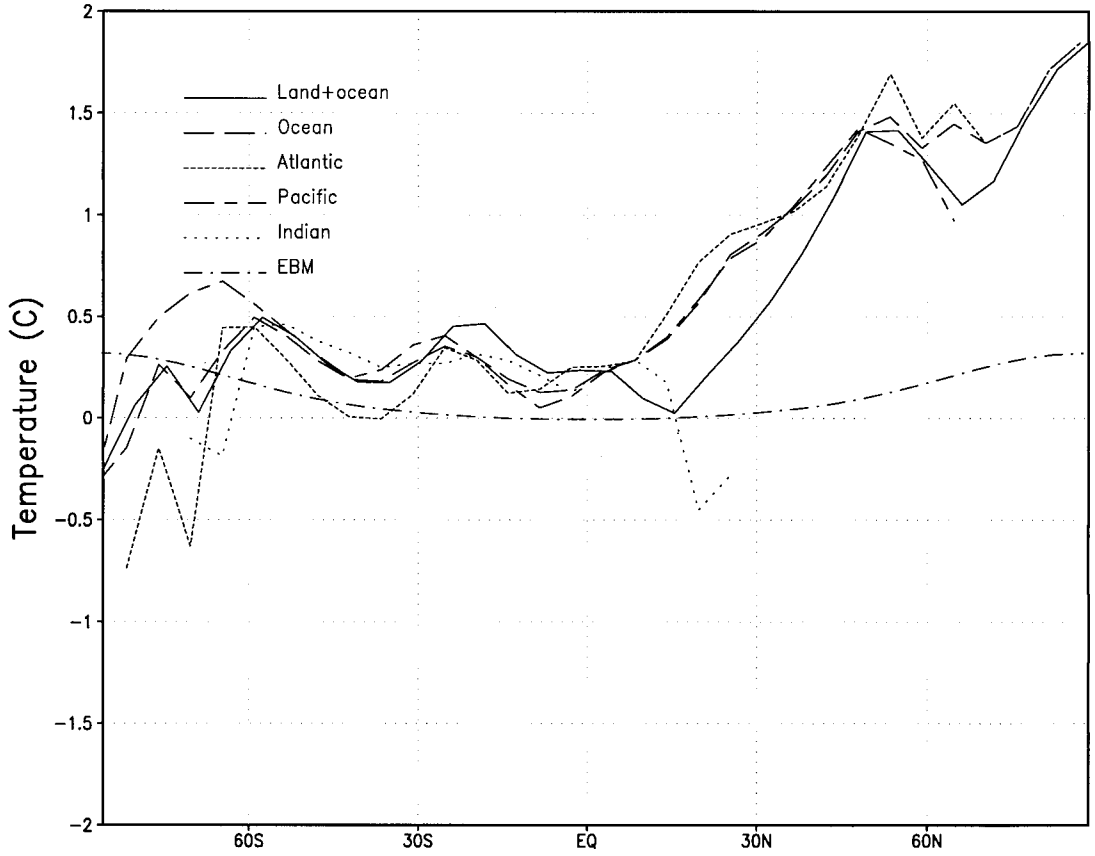

FIG. 16. Zonally averaged surface temperature change (Eemian minus control run) for the three ocean basins and the global ocean as simulated by our GCM (corrected to adjust for the radiative forcing due to the different CO_2 concentration) compared to the surface temperature change obtained by a linear EBM (°C).

(Harrison et al. 1995) and 9 kyr BP (Kutzbach and Guetter 1986; Mitchell et al. 1988; Kutzbach and Gallimore 1988); however, drier conditions over eastern Asia have been reported in a more recent simulation for the early Holocene (Kutzbach et al. 1998). In addition, the simulated globally averaged precipitation is reduced by 1%, contrary to the idea that enhanced precipitation in the Tropics due to intensified monsoons leads to enhanced precipitation on land as a whole [Keigwin and Boyle (1985)]. Duplessy et al. (1984) present deep-sea $\delta^{13}C$ data that also challenge this conclusion; their result suggests perhaps less carbon stored on land during the Eemian. Our results are more ambiguous for two reasons. First, the 1% decrease might not be detectable in the marine $\delta^{13}C$ record. For example, terrestrial carbon decreases during the LGM may have been 20%–25% or more (Crowley 1995), leading to a 0.3‰–0.4‰ change in marine $\delta^{13}C$. Duplessy et al. (1984) found a 0.1‰ change in the Eemian, which would translate into about a 5% change in carbon storage on land. If there is any linkage between total precipitation and total carbon storage (a reasonable hypothesis), a 1% decrease in precipitation should therefore cause only about a 0.02‰ change in the marine $\delta^{13}C$ record. This small change cannot be detected at a significant level in the marine record.

A further problem involves the fact that our model utilized a CO_2 level about 60 ppmv less than the control. Boer (1993) demonstrated that for a doubling of CO_2 there is a 1%–2% increase in global precipitation. If this same relationship holds for lower CO_2 levels, we would expect that all or part of our 1% decrease could be an artifact of the lower CO_2 levels in the Eemian run. This reasoning would suggest that perhaps a safer way to interpret our precipitation results is that it is difficult to make a case for significant changes in mean annual precipitation on land due to altered Milankovitch forcing. This tentative conclusion is still at variance with some geological inferences, which, like the temperature data, may be biased by spatial sampling distribution and hence require more testing with additional simulations.

As a consequence of the decreased freshwater flux at mid- and high northern latitudes of the Pacific and Atlantic Ocean basins, a slight intensification of the meridional overturning circulation in both oceans is found at the Eemian, resulting in an enhanced global northward heat transport by 10% at 15°N. The ocean circulation response in the Atlantic Ocean contrasts with the

evidence from δ^{13}C data (Duplessy et al. 1984; Duplessy and Shackleton 1985), which suggests reduced NADW formation/enhanced AABW, which in turn could be coupled responses. Enhanced AABW was also found in a sea ice–ocean model forced by the energy balance model response to the insolation perturbation at the Eemian (Kim et al. 1998). However, our result is comparable to the evidence from Cd/Ca and δ^{13}C data in more recent high-resolution records from the North Atlantic (Oppo et al. 1997; Adkins et al. 1997) suggesting NADW levels similar to Holocene levels in midsubstage 5e; the δ^{13}C and Cd/Ca data disagree in early stage 5e. The reasons for the differences in the datasets require further analysis; they may be methodological, the cores may be sampling different parts of the water column, or there may be real differences in circulation patterns between early and midstage 5e.

Finally, our results suggest globally averaged temperatures were not significantly higher in the Eemian than in the mid–twentieth century. This conclusion is supported by the agreement between simulated and Climate: Long-Range Investigation Mapping and Prediction (CLIMAP Project Members 1984) reconstructed SSTs (Montoya et al. 1998), and agrees with results of a simulation for 6 kyr BP in that both show ''no indication for a global climatic optimum'' (Kutzbach et al. 1998), but contradicts general assumptions. These could arise from a misinterpretation of the paleodata due to a bias in their spatial distribution [there is evidence also for warmer temperatures than present in the Southern Hemisphere, e.g., in East Antarctica (Jouzel et al. 1987), but these events might not have been globally synchronous (Crowley 1990)], or to an incorrect interpretation of annual average conditions from summer indicators (e.g., vegetation may be more sensitive to summer warming due to Milankovitch forcing whereas in the winter plants are almost dormant). Alternatively, our GCM could be underestimating the response. We emphasize the importance of carrying out similar approaches with other climate models, in particular those including interactive vegetation, which could potentially amplify the response to the insolation perturbation, and of obtaining a better sampling from regions other than northwestern Europe in order to assess this possibility.

Acknowledgments. We thank D. Schriever and M. Lautenschlager for supporting us with the simulations for the last interglacial and S.-Y. Kim for providing us with the EBM results. M. Montoya thanks also E. Zorita and S. Rahmstorf for valuable discussion, R. Voss and U. Cubasch for discussion concerning technical details of the model, and J.-S. von Storch for her help in the analysis of the ocean data. Finally, we thank J. Kutzbach and another anonymous reviewer for their valuable comments. M. Montoya was supported by a grant of the Dirección General de Investigación Científica y Técnica (Spain). H. von Storch was supported by EU Project MILLENIA. T. J. Crowley was supported by National Science Foundation Grant ATM-9529109.

APPENDIX

Univariate Recurrence Analysis

Two random variables X, Y are said to be p recurrent if the probability that Y be greater than the mean value of X is equal to p [$P(Y > \overline{X}) = p$]. Therefore, p is a measure of the overlap of the distributions of the X and Y. If $\overline{X} = \overline{Y}$, then $p = 0.5$, and their distributions are coincident and physically indistinguishable; the overlap decreases as p deviates from 0.5. Values of p close to 0 (1) imply that the distribution of X and Y seldom overlap and that Y is generally much larger (smaller) than X.

In climate modeling applications, X usually represents the sample space (i.e., the list of possible outcomes) of a given variable in a control climate experiment at a given location and and Y the corresponding sample space in an anomalous climate, obtained by altered boundary conditions (in our case, the control and Eemian runs, respectively). At each time step, one realization of X and Y is obtained; for a finite time period, an ensemble of realizations are collected from which p can be estimated at a given point. If X and Y are two normally distributed random variables with mean values $\overline{X}$ and $\overline{Y}$ and standard deviation σ, then p is given by

$$p = F\left(\frac{\overline{X} - \overline{Y}}{\sigma}\right), \tag{A1}$$

where F is the distribution function of the standard normal distribution $N(0, 1)$. Here, p represents the local level of recurrence and is a measure of of the strength of the effect of the anomalous boundary conditions.

REFERENCES

Adkins, J. F., E. A. Boyle, L. Keigwin, and E. Cortijo, 1997: Variability of the North Atlantic thermohaline circulation during the last interglacial period. *Nature,* **390,** 154–156.

Barnola, J. M., D. Raynaud, Y. S. Korotkevich, and C. Lorius, 1987: Vostok ice core provides 160,000-year record of atmospheric CO_2, *Nature,* **329,** 408–414.

Berger, A. L., 1978: Long-term variations of daily insolation and Quaternary climatic changes. *J. Atmos. Sci.,* **35,** 2362–2367.

Bloom, A. L., J. M. A. Chappel, W. S. Broecker, R. K. Matthews, and K. J. Mesolella, 1974: Quaternary sea-level fluctuations on a tectonic coast: New ^{230}Th/^{234}U dates from the Huon peninsula. *Quat. Res.,* **4,** 185–205.

Boer, G., 1993: Climate change and the regulation of the surface moisture and energy budgets. *Climate Dyn.,* **8,** 225–239.

Budyko, M. I., and Y. A. Izrael, 1991: *Anthropogenic Climatic Change.* The University of Arizona Press, 406 pp.

Bush, A. B., and G. H. Philander, 1998: The role of ocean–atmosphere interactions in tropical cooling during the last glacial maximum. *Science,* **279,** 1341–1344.

CLIMAP Project Members, 1984: The last interglacial ocean, *Quat. Res.,* **21,** 123–224.

Crowley, T. J., 1990: Are there any satisfactory analogs for a future greenhouse warming? *J. Climate,* **3,** 1282–1292.

——, 1995: Ice age terrestrial carbon changes revisited. *Global Biogeochem. Cycles,* **9,** 377–389.
——, and K.-Y. Kim, 1994: Milankovitch forcing of the last interglacial sea level. *Science,* **265,** 1566–1568.
——, and S. K. Baum, 1997: Effect of vegetation on an ice age climate model simulation. *J. Geophys. Res.,* **102,** 16 463–16 480.
Cubasch, U., K. Hasselmann, H. Höck, E. Maier-Reimer, U. Mikolajewicz, B. Santer, and R. Sausen, 1992: Time-dependent greenhouse warming computations with a coupled ocean–atmosphere model. *Climate Dyn.,* **8,** 55–69.
——, B. D. Santer, A. Hellbach, G. C. Hegerl, H. Hock, E. Maier-Reimer, U. Mikolajewicz, A. Stossel, and R. Voss, 1994: Monte Carlo climate change forecasts with a global coupled ocean–atmosphere model. *Climate Dyn.,* **10,** 1–19.
——, G. C. Hegerl, A. Hellbach, H. Hock, U. Mikolajewicz, B. D. Santer, and R. Voss, 1995: A climate change simulation starting from 1935. *Climate Dyn.,* **11,** 75–84.
de Beaulieu, J. L., and M. Reille, 1984: A long upper Pleistocene pollen record from Les Echets, near Lyon, France. *Boreas,* **133,** 111–132.
——, and ——, 1992: Long Pleistocene pollen sequences from the Velay Plateau (Massif Central, France), I. *Veg. Hist. Archaeobot.,* **1,** 233–242.
de Noblet, N., P. Braconnot, S. Joussaume, and V. Masson, 1996: Sensitivity of simulated Asian and African summer monsoons to orbitally induced variations in insolation 126, 115 and 6 kBP. *Climate Dyn.,* **12,** 589–603.
Dong, B., and P. J. Valdes, 1998: Simulations of the last glacial maximum climates using a general circulation model: Prescribed versus computed sea surface temperatures. *Climate Dyn.,* **14,** 571–591.
Duplessy, J. C., and N. J. Shackleton, 1985: Response of global deep-water circulation to Earth's climatic change 135,000–107,000 years ago. *Nature,* **316,** 500–506.
——, ——, R. K. Matthews, W. Prell, W. F. Ruddiman, M. Caralp, and C. H. Hendy, 1984: ^{13}C record of benthic foraminifera in the last interglacial ocean: Implications for the carbon cycle and the global deep water circulation. *Quat. Res.,* **21,** 225–243.
Egger, J., 1997: Flux correction: Tests with a simple ocean-atmosphere model. *Climate Dyn.,* **13,** 285–292.
Follieri, M., and L. Sadori, 1988: 250,000 year pollen record from Valle di Castiglione (Roma). *Pollen Spores,* **30,** 329–356.
Fung, I., A. Lacis, D. Rind, S. Lebedeff, R. Ruedyand, and G. Russell, 1988: Global climate changes as forecast by Goddard Institute for Space Studies three-dimensional model. *J. Geophys. Res.,* **93,** 9341–9364.
Ganopolski, A., S. Rahmstorf, V. Petoukhov, and M. Claussen, 1997: Simulation of modern and glacial climates with a coupled global climate model. *Nature,* **391,** 350–356.
——, C. Kubatzki, M. Claussen, V. Brovkin, and V. Petoukhov, 1998: The influence of vegetation–atmosphere–ocean interaction on climate during the mid-Holocene. *Science,* **280,** 1916–1919.
Hall, N. M. J., and P. J. Valdes, 1997: A GCM simulation of the climate 6000 years ago. *J. Climate,* **10,** 3–17.
Harrison, S. P., J. E. Kutzbach, C. E. Prentice, P. J. Behling, and M. T. Sykes, 1995: The response of Northern Hemisphere extratropical climate and vegetation to orbitally induced changes in insolation during the last interglaciation. *Quat. Res.,* **43,** 174–184.
Hellerman, S., and M. Rosenstein, 1983: Normal monthly wind stress over the World Ocean with error estimates. *J. Phys. Oceanogr.,* **13,** 1093–1104.
Hewitt, C. D., and J. F. B. Mitchell, 1996: GCM simulations of the climate of 6kyr BP: Mean changes and interdecadal variability. *J. Climate,* **9,** 3505–3529.
——, and ——, 1998: A fully coupled GCM simulation of the climate of the mid-Holocene. *Geophys. Res. Lett.,* **25,** 361–364.
Joussaume, S., and P. Braconnot, 1997: Sensitivity of paleoclimate simulation results to season definitions. *J. Geophys. Res.,* **102,** 1943–1956.
Jouzel, J., C. Lorius, J. R. Petit, C. Genthon, N. I. Barkov, V. M. Kotlyakov, and V. M. Petrov, 1987: Vostok ice core: A continuous isotope temperature record over the last climatic cycle (160,000 years). *Nature,* **329,** 403–408.
Keigwin, L., and E. A. Boyle, 1985: Carbon isotopes in deep-sea foraminifera: precession and changes in low-latitude biomass. *The Carbon Cycle and Atmospheric C0$_2$: Natural Variations Archean to Present, Geophys. Monogr.,* No. 32, Amer. Geophys. Union, 319–328.
Kellogg, W., 1977: Effects of human activities on global climate. WMO Rep. 486, 47 pp.
Kim, S. Y., T. J. Crowley, and A. Stössel, 1998: Local orbital forcing of Antarctic climate change during the last interglacial. *Science,* **280,** 728–730.
Ku, T. L., M. A. Kimmel, W. H. Easton, and T. J. O'Neil, 1974: Eustatic sea level 120,000 years ago on Oahu, Hawaii. *Science,* **183,** 959–962.
Kubatzki, C., and M. Claussen, 1998: Simulation of the global biogeophysical interactions during the Last Glacial Maximum. *Climate Dyn.,* **14,** 461–471.
Kutzbach, J. E., and P. J. Guetter, 1986: The influence of changing orbital parameters and surface boundary conditions on climate simulations for the past 18,000 years. *J. Atmos. Sci.,* **43,** 1726–1759.
——, and R. Gallimore, 1988: Sensitivity of a coupled atmosphere/mixed layer ocean model to changes in orbital forcing at 9000 BP. *J. Geophys. Res.,* **93,** 801–821.
——, and Z. Liu, 1997: Response of the African monsoon to orbital forcing and ocean feedbacks in the middle Holocene. *Science,* **278,** 440–443.
——, R. G. Gallimore, and P. J. Guetter, 1991: Sensitivity experiments on the effects of orbitally-caused insolation changes on the interglacial climate of high northern latitudes. *Quat. Int.,* 223–229.
——, G. Bonan, J. Foley, and S. P. Harrison, 1996: Vegetation and soil feedbacks on the response of the African monsoon to orbital forcing in the early to middle Holocene. *Nature,* **384,** 623–626.
——, R. Gallimore, S. Harrison, P. Behling, R. Selin, and F. Laarif, 1998: Climate and biome simulations for the past 21,000 years. *Quat. Sci. Rev.,* **17,** 473–506.
Levitus, S., 1982: *Climatology Atlas of the World Ocean.* NOAA Prof. Paper No. 13, U.S. Government Printing Office, 173 pp.
LIGA Members, 1991: Report of 1st discussion group: The last interglacial in high latitudes of the northern hemisphere: Terrestrial and marine evidence. *Quat. Int.,* **10–12,** 9–28.
Maier-Reimer, E., U. Mikolajewicz, and K. Hasselmann, 1993: Mean circulation of the Hamburg LSG OGCM and its sensitivity to the thermohaline surface forcing. *J. Phys. Oceanogr.,* **23,** 731–757.
Manabe, S., M. J. Spelman, R. J. Stouffer, and K. Bryan, 1991: Transient responses of a coupled ocean–atmosphere model for gradual changes of atmospheric CO_2. Part I: Annual mean response. *J. Climate,* **4,** 785–818.
——, ——, and ——, 1992: Transient responses of a coupled ocean–atmosphere model for gradual changes of atmospheric CO_2. Part II: Seasonal response. *J. Climate,* **5,** 105–126.
Mesolella, K. J., R. K. Matthews, W. S. Broecker, and D. L. Thurber, 1969: The astronomical theory of climatic change: Barbados data. *J. Geol.,* **77,** 250–274.
Mitchell, J. F. B., N. S. Grahame, and K. J. Needham, 1988: Climate simulations for 9000 years before present: Seasonal variations and effects on the Laurentide ice sheet. *J. Geophys. Res.,* **93,** 8283–8303.
Monin, A. S., 1986: *Introduction to the Theory of Climate.* Reidel, 261 pp.
Montoya, M., T. J. Crowley, and H. von Storch, 1998: Temperatures at the last interglacial simulated by means of a coupled general circulation model. *Paleoceanography,* **13,** 170–177.
Oppo, D. W., M. Horowitz, and S. Lehman, 1997: Marine core evidence for a sharp decrease in deep water production during

Termination II and a relatively stable MIS 5e (Eemian). *Paleoceanography,* **12,** 51–64.
Petit-Maire, N., 1994: Natural variability of the Asian, Indian and African monsoons over the last 130 ka. *Global Precipitations and Climate Change,* M. Desbois and F. Désalmand, Eds., Vol. 1, No. 26, NATO ASI Series, Springer-Verlag, 3–25.
Pons, A., and M. Reille, 1988: The Holocene and upper Pleistocene pollen record from Padul (Granada, Spain). *Palaeogeogr., Palaeoclim., Palaeoecol.,* **66,** 243–263.
Prell, W. L., and J. E. Kutzbach, 1987: Monsoon variability over the last 150,000 years. *J. Geophys. Res.,* **92,** 8411–8425.
Roeckner, E., and Coauthors, 1992: Simulation of the present day climate with the ECHAM model: Impact of model physics and resolution. Max-Planck-Institut für Meteorologie Rep. 93, 178 pp. [Available from Max-Planck-Institut für Meteorologie, Bundesstrasse 55, D-20146 Hamburg, Germany].
Rollins, H. B., J. B. Richardson, and D. H. Sandweiss, 1986: The birth of El Niño: Geoarcheological evidence and implications. *Geoarcheology,* **1,** 3–15.
Royer, J. F., F. Deque, and P. Pestiaux, 1984: A sensitivity experiment to astronomical forcing with a spectral GCM: Simulation of the annual cycle at 125 000 and 115 000 BP. *Milankovitch and Climate,* A. Berger et al., Eds., NATO ASI Series, Reidel, 733–736.
Sandweiss, D. H., J. B. Richardson, E. J. Reitz, H. B. Rollins, and K. A. Maasch, 1996: Geoarcheological evidence from Peru for a 5000 year BP onset of El Niño. *Science,* **273,** 1521–1533.
Sausen, R., K. Barthel, and K. Hasselmann, 1988: Coupled ocean–atmosphere models with flux corrections. *Climate Dyn.,* **2,** 154–163.
Shabalova, M., and G. P. Können, 1995: Climate change scenarios: Comparison of paleoreconstructions with recent temperature changes. *Climatic Change,* **29,** 409–428.
Texier, D., and Coauthors, 1997: Quantifying the role of biosphere–atmosphere feedbacks in climate change: Coupled model simulations for 6000 years BP and comparison with paleodata for northern Eurasia and northern Africa. *Climate Dyn.,* **13,** 865–882.
Tzedakis, P. C., 1993: Long-term trees population in northwest Greece through multiple Quaternary climatic cycles. *Nature,* **364,** 437–440.
von Storch, H., and F. Zwiers, 1998: *Statistical Analysis in Climate Research.* Cambridge University Press, 528 pp.
von Storch, J.-S., V. Kharin, U. Cubasch, G. C. Hegerl, D. Schriever, H. von Storch, and E. Zorita, 1997: A 1260-year control integration with the coupled ECHAM1/LSG general circulation model. *J. Climate,* **10,** 1525–1543.
Watts, W. A., 1985: A long pollen record from Lagui di Monticchio, southern Italy: A preliminary account. *J. Geol. Soc. London,* **142,** 491–499.
Wijmstra, T. A., 1969: Palynology of the first 30 meters of a 120 m deep section in Northern Greece. *Acta Bot. Neerl.,* **18,** 511–527.
Woillard, G. M., 1978: Grande Pile peat bog: A continuous pollen record for the last 140,000 years. *Quat. Res.,* **9,** 1–21.
Woodruf, S. D., R. J. Slutz, R. L. Jenne, and P. M. Steurer, 1987: A comprehensive ocean–atmosphere data set. *Bull. Amer. Meteor. Soc.,* **68,** 1239–1250.
Zubakov, V. A., and I. I. Borzenkova, 1990: *Global Palaeoclimate of the Late Cenozoic.* Elsevier, 453 pp.